



Elliptical particle suspensions in Couette flow

Xuechao Liu , Haibo Huang *, and Xi-yun Lu 

*Department of Modern Mechanics, University of Science and Technology of China,
Hefei 230026, China*



(Received 8 September 2021; accepted 4 April 2022; published 20 April 2022)

The rheological properties and microstructure of neutrally buoyant elliptical particle suspensions are studied using the immersed boundary-lattice Boltzmann method. For dilute suspensions containing only one particle, with the increase of aspect ratio Ar , the particle ceases to rotate due to the inertia at a critical aspect ratio Ar_c , and the value of Ar_c decreases with increasing Re . The inertia-induced rotation arrest causes a nonmonotonic variation of particle alignment with the flow direction, and thence the relative viscosity, with increasing Ar , for a fixed Re . The relative viscosity first decreases, with increasing Ar due to the increasing alignment (on average) of tumbling particles; however, rotation arrest leads to a subsequent increase in the relative viscosity for $Ar > Ar_c$. This nonmonotonic variation persists over the entire range of Re and Ar examined here. For dense suspensions containing multiple particles, with increasing Ar , particles align more with the flow, but the orientation becomes almost constant when Ar is greater than a threshold Ar_t . Smaller values of Ar_t are observed for higher Re . Meanwhile, η_r decreases due to particle alignment for $Ar < Ar_t$ and then increases due to high particle-particle interaction for $Ar > Ar_t$. Further, the contributions of stresslet (S), particle acceleration stress (P), and Reynolds stress (R) on η_r and the first normal stress difference N_1 are analyzed. In addition to the major contribution of stresslet, Reynolds stress contributes more as Ar increases at high Re . In addition, the microstructure and the probability density functions of lateral velocity (U_y) and angular velocity (ω_p) are also analyzed. Our results may be helpful to understand the rheological properties of nonspherical particle suspensions.

DOI: [10.1103/PhysRevFluids.7.044303](https://doi.org/10.1103/PhysRevFluids.7.044303)

I. INTRODUCTION

Suspensions of particles are ubiquitous in nature and industries. Understanding the rheological properties of suspensions is important in many industrial design processes, such as papermaking [1] and waste slurries [2]. Usually, a constitutive equation relating shear stress τ to the strain rate $\dot{\gamma}$ [3] is used to quantitatively describe the deformation and flow behavior of suspensions. In the past research, the effective viscosity $\eta = \tau/\dot{\gamma}$ is commonly used. The relative viscosity η_r is defined as $\eta_r = \eta_s/\eta_0$, where η_s is the effective viscosity of the suspensions and η_0 is the viscosity of suspending liquid. For non-Brownian neutrally buoyant particle suspensions, η_r depends on the particle concentration ϕ and Reynolds number Re by the dimensional analysis, i.e., $\eta_r = f(\phi, Re)$ [2], where $Re = \rho\dot{\gamma}a^2/\mu$, ρ is the fluid density, $\dot{\gamma}$ is the shear rate of the flow, a is the particle size, and μ is the dynamic viscosity.

In the Stokesian domain, the effect of Re is negligible and η_r is only a function of ϕ . Numerous studies have been performed to understand the correlation between η_r and ϕ . For dilute suspensions, Einstein [4] first deduced the classical equation analytically, i.e., $\eta_r = 1 + [\eta]\phi$, where $[\eta]$ is the

*huanghb@ustc.edu.cn

intrinsic viscosity and $[\eta] = 2.5$ for rigid spheres. In the derivation, the fluid inertial effect and the hydrodynamic interactions between particles are neglected. Jeffery [5] analytically extended Einstein's results to spheroidal particle suspensions. He investigated the motion of a spheroidal particle in dilute shearing suspension and found that several terminal motion modes are possible. Each mode corresponds to a different $[\eta]$. To determine which mode is the actual terminal mode, he hypothesized that "The particle will tend to adopt that motion which, of all the motions possible under the approximated equations, corresponds to the least dissipation of energy." To consider the hydrodynamic interactions, Batchelor and Green [6] further proposed $\eta_r = 1 + [\eta]\phi + B\phi^2$, where $B = 6.95$ for non-Brownian suspensions in pure straining flow [7]. For more dense suspensions, Krieger and Dougherty [8] derived $\eta_r = (1 - \phi/\phi_m)^{-[\eta]\phi_m}$, where ϕ_m is the maximum packing concentration of particles. In addition to the analytical work, many numerical simulations [9–11] and experiments [3,12] have been carried out to study the microstructure and rheology of Stokes-flow particle suspension.

In the inertial domain, the effect of Re should be considered. By including the term $O(Re^{\frac{3}{2}})$, Lin *et al.* [13] incorporated the inertial effect into the Einstein viscosity law. Subramanian *et al.* [14] calculate the rheological properties of a dilute emulsion of nearly spherical drops at $O(\phi Re^{3/2})$. For nonspherical particles, Subramanian and co-workers have done a great deal of work to investigate the effect of inertia on the orientation dynamics of spheroids or fiber [15–17]. Subramanian and Koch [18] investigated the inertial effect on the orientation of nearly spherical particles in shear flow, and they concluded that a neutrally buoyant prolate spheroid migrates toward the direction of vorticity due to the fluid inertia effect. However, their subsequent results showed that this is incorrect [16]. Dabade *et al.* [16] evaluate the drifts in orientation and calculate the intrinsic viscosity coefficients at $O(Re)$ and $O(St)$ as a function of the particle aspect ratio for both prolate and oblate spheroids. Their results show that fluid inertia drives a prolate spheroid towards a tumbling motion in the flow-gradient plane in spite of the initial orientations and aspect ratios. The theoretical approach is a useful tool to study the rheology of suspensions, but it is limited to small Re and simple geometries [19].

Many numerical simulation methods have been used to study the effect of inertia on the particle suspension, including the lattice Boltzmann method [20], the force coupling method [21], and the curvilinear immersed-boundary method [19]. Kulkarni and Morris [22] and Haddadi and Morris [20] studied the microstructure and rheology of neutrally buoyant spherical particle suspensions, and the rheological properties including relative viscosity, normal stress differences, and particle pressure are investigated in detail with finite inertia. For a spheroidal particle, the inertia of both the fluid and the particle can influence the particle motion and hence the rheology. The studies of Qi and Luo [23], Huang *et al.* [24], and Rosén *et al.* [25] show that a prolate spheroid can rotate in tumbling, log-rolling (spinning), kayaking, and steady states depending on the aspect ratio, the Reynolds number, and the initial orientation. For an oblate spheroid, tumbling, log-rolling, and steady states are observed [26]. Further, Rosén *et al.* [27] studied the effect of particle inertia on the rotational motion of a spheroid particle in shear flow. Using the lattice Boltzmann method, Huang *et al.* [28] investigated the shear viscosity of dilute suspensions of spheroid particles, and they found that the viscosity changes linearly at the low Re regime and nonlinearly at the high Re regime. Daghooghi and Borazjani [19] numerically investigated the rheology properties of the ellipsoid suspension. They found that the contribution of particle acceleration stress and Reynolds stress on the normal stress difference cannot be ignored for nonspherical particles at finite inertia. However, in their simulations, there is only one ellipsoid inside a periodic domain, and the particle-particle interactions are negligible.

Despite the above numerous studies, the effect of inertia on the rheology of spheroid particle suspensions is limited, and the effect of particle rotational motion on the rheology is not clear at finite inertia. Two-dimensional simulation is a useful and efficient tool for understanding the hydrodynamics dynamics of particle suspensions. Through a large number of two-dimensional simulations for a sufficiently large range of parameters, we may draw conclusive inferences about

scaling trends. Besides, most of the qualitative results obtained in a two-dimensional numerical solution can be generalized to three-dimensional flows, and previous extensive studies support this viewpoint [29]. For example, Aidun *et al.* [30] studied the rotational motion of the two-dimensional (2D) elliptical particle, and they found that the transition from a time-periodic to a steady state is through a saddle-node bifurcation. The period of oscillation near a transition is proportional to $|p - p_c|^{-1/2}$, where p is any parameter in the flow. The latter studies for 3D flows found a similar scaling law [25].

Hence, in this study, two-dimensional simulations are performed to investigate the microstructure and rheology properties of the elliptical particle suspensions with many particles using the immersed boundary lattice Boltzmann method (IB-LBM). Here the effects of particle shape, particle concentration, and Reynolds number are investigated in detail, and the relation between the viscosity and the particle orientation is investigated. Meanwhile, the contributions of three components, i.e., stresslet, particle acceleration stress, and Reynolds stress to the rheological properties are discussed. Only the tumbling motion is considered in this work due to the limit of 2D simulation. The method and physical problem are introduced in Sec. II. Validation of the program is presented in Sec. III. Results and discussion are presented in Sec. IV. Finally, conclusions are summarized in Sec. V.

II. METHOD AND PHYSICAL PROBLEM

A. Lattice-Boltzmann method

Here the governing equations for fluid flows are the incompressible Navier-Stokes equations [Eq. (1)],

$$\frac{\partial \mathbf{u}}{\partial t} + \mathbf{u} \cdot \nabla \mathbf{u} = -\frac{1}{\rho} \nabla p + \frac{\mu}{\rho} \nabla^2 \mathbf{u} + \mathbf{f}_b, \quad (1a)$$

$$\nabla \cdot \mathbf{u} = 0, \quad (1b)$$

where \mathbf{u} is the velocity, p is the pressure, ρ is the density of the fluid, μ is the dynamic viscosity, and \mathbf{f}_b is the Eulerian momentum force on the surrounding fluid due to the immersed boundary, as constrained by the no-slip boundary condition. The motion of the particle is controlled by Newton's second law.

The lattice Boltzmann method (LBM) is used to solve the fluid flow governed by the incompressible Navier-Stokes equations, and the direct-forcing immersed boundary method (IB) is applied to treat flow-structure interaction [31].

The evolution equation in the LBM is

$$f_\alpha(\mathbf{x} + \mathbf{e}_\alpha \delta t, t + \delta t) - f_\alpha(\mathbf{x}, t) = -\frac{1}{\tau} [f_\alpha(\mathbf{x}, t) - f_\alpha^{\text{eq}}(\mathbf{x}, t)] + \delta t F_\alpha,$$

where τ is the relaxation time and $f_\alpha(\mathbf{x}, t)$ is the particle distribution function. $f_\alpha^{\text{eq}}(\mathbf{x}, t)$ is the equilibrium particle distribution function, and it is written as

$$f_\alpha^{\text{eq}}(\mathbf{x}, t) = \rho \omega_\alpha \left[1 + \frac{\mathbf{e}_\alpha \cdot \mathbf{u}}{c_s^2} + \frac{(\mathbf{e}_\alpha \cdot \mathbf{u})^2}{2c_s^4} - \frac{\mathbf{u}^2}{2c_s^2} \right]. \quad (2)$$

The last term F_α represents the effect of external force and is calculated as [32]

$$F_\alpha = \left(1 - \frac{1}{2\tau} \right) \omega_\alpha \left[\frac{\mathbf{e}_\alpha - \mathbf{u}}{c_s^2} + \frac{(\mathbf{e}_\alpha \cdot \mathbf{u})}{c_s^4} \mathbf{e}_\alpha \right] \cdot \mathbf{F}, \quad (3)$$

where \mathbf{F} is the macroscopic external force term. The macroscopic density ρ and macroscopic velocity can be obtained through

$$\rho = \sum_{\alpha=0}^8 f_\alpha \quad (4)$$

and

$$\rho u_i = \sum_{\alpha=0}^8 e_{i\alpha} f_\alpha + \frac{F_i \delta t}{2\rho}, \quad (5)$$

respectively.

In our LBM simulations, the D2Q9 velocity model is adopted. The discrete velocities \mathbf{e}_α in the D2Q9 model are defined as

$$\mathbf{e}_\alpha = \begin{cases} 0, & \alpha = 0, \\ c \left(\cos \left[\frac{(\alpha-1)\pi}{4} \right], \sin \left[\frac{(\alpha-1)\pi}{4} \right] \right), & \alpha = 1 - 4, \\ \sqrt{2}c \left(\cos \left[\frac{(\alpha-1)\pi}{4} \right], \sin \left[\frac{(\alpha-1)\pi}{4} \right] \right), & \alpha = 5 - 8. \end{cases} \quad (6)$$

The corresponding weight parameters ω_α are

$$\omega_\alpha = \begin{cases} \frac{4}{9}, & \alpha = 0, \\ \frac{1}{9}, & \alpha = 1 - 4, \\ \frac{1}{36}, & \alpha = 5 - 8. \end{cases} \quad (7)$$

The lattice speed c is given by $c = \frac{\delta x}{\delta t}$, where δx is the lattice size and δt is the time step. $c_s^2 = \frac{c^2}{3}$ is the lattice sound speed.

In the immersed boundary method, the particle boundary is discretized into small elements by many Lagrange points. The boundary force on a Lagrange point, e.g., \mathbf{x}_b , can be calculated by

$$\mathbf{F}(\mathbf{x}_b, t) = 2\rho \frac{\mathbf{U}^d - \mathbf{u}^{\text{noF}}(\mathbf{x}, t + \delta t)}{\delta t}, \quad (8)$$

where \mathbf{U}^d and \mathbf{u}^{noF} are the desired velocity and the unforced velocity at the point at $t + \delta t$. The velocity \mathbf{U}^d at the Lagrange point \mathbf{x}_b is

$$\mathbf{U}^d = \mathbf{U}_p + \boldsymbol{\omega}_p \cdot \mathbf{r}, \quad (9)$$

where \mathbf{U}_p and $\boldsymbol{\omega}_p$ are the translational velocity and angular velocity of the particle, respectively. \mathbf{r} is the vector from the particle center to the Lagrange point. \mathbf{u}^{noF} is interpolated from neighboring Eulerian points, i.e.,

$$\mathbf{u}^{\text{noF}} = D(\mathbf{x}_{i,j} - \mathbf{x}_b) \mathbf{u}, \quad (10)$$

where $\mathbf{x}_{i,j}$ denotes the Eulerian points surrounding the Lagrange point \mathbf{x}_b . $D()$ represents a discrete δ function,

$$D(\mathbf{x}_{i,j} - \mathbf{x}_b) = \frac{1}{(\delta x)^2} d_{\delta x} \left(\frac{x_i - x_b}{\delta x} \right) d_{\delta x} \left(\frac{y_j - y_b}{\delta x} \right), \quad (11)$$

with

$$d_{\delta x}(r) = \begin{cases} \frac{1}{8}(3 - 2r + \sqrt{1 + 4r - 4r^2}), & 0 \leq r < 1, \\ \frac{1}{8}(5 - 2r + \sqrt{-7 + 12r - 4r^2}), & 1 \leq r < 2, \\ 0, & r \geq 2. \end{cases} \quad (12)$$

The force density on an Eulerian node can be calculated by

$$\mathbf{F}(\mathbf{x}_{i,j}, t) = \sum_{\mathbf{x}_b} D(\mathbf{x}_{i,j} - \mathbf{x}_b) \mathbf{F}(\mathbf{x}_b, t) \Delta S_b, \quad (13)$$

where ΔS_b is the boundary segment length including Lagrange point \mathbf{x}_b .

The total hydrodynamic force (\mathbf{F}_h) and torque (\mathbf{Tor}_h) acting on the particle are

$$\mathbf{F}_h = - \sum_{\mathbf{x}_b} \mathbf{F}(\mathbf{x}_b, t) \Delta S_b + M_f \frac{d\mathbf{U}_p}{dt}, \quad (14a)$$

$$\mathbf{Tor}_h = - \sum_{\mathbf{x}_b} \mathbf{r} \times \mathbf{F}(\mathbf{x}_b, t) \Delta S_b + I_f \frac{d\boldsymbol{\omega}_p}{dt}, \quad (14b)$$

where M_f and I_f are the mass and inertia moment of the fluid occupied by the particle representing the added mass effect, which should be considered for a moving body [31].

In numerical simulations, when two particles are very close to each other or a particle is close to a wall, a short-range repulsive force, such as the spring force model [33] and the lubrication force model [34], should be introduced to prevent overlapping. Here, the lubrication force is not used and only the repulsive spring force is included, and the repulsive force is [33]

$$\mathbf{F}_R = \begin{cases} 0 & \text{if } |\mathbf{x}_s| > s, \\ \frac{C}{\epsilon_w} \left(\frac{|\mathbf{x}_s| - s}{s} \right) \frac{\mathbf{x}_s}{|\mathbf{x}_s|} & \text{if } |\mathbf{x}_s| < s, \end{cases} \quad (15)$$

where s is the threshold distance, ϵ_w is the stiffness parameter, C is the relative force scale, and \mathbf{x}_s denotes the vector between the two nearest points on two particles or between the particle and the wall. The torque acting on the particle due to the repulsive force is

$$\mathbf{Tor}_R = \mathbf{r} \times \mathbf{F}_R, \quad (16)$$

where \mathbf{r} is the vector from the particle center to the point on the particle surface at which the repulsive force is imposed.

The total force and torque acting on the particle are

$$\mathbf{F}_p = \mathbf{F}_h + \mathbf{F}_R, \quad (17a)$$

$$\mathbf{Tor}_p = \mathbf{Tor}_h + \mathbf{Tor}_R. \quad (17b)$$

The translational and rotational motions of the particle are controlled by Newton's law,

$$M_p \frac{d\mathbf{U}_p}{dt} = \mathbf{F}_p, \quad (18a)$$

$$I_p \frac{d\boldsymbol{\omega}_p}{dt} = \mathbf{Tor}_p, \quad (18b)$$

where M_p and I_p are the mass and inertia moment of the particle, respectively. After the total force and torque acting on the particles are calculated, the particle translational velocity \mathbf{U}_p , position \mathbf{X} , angular velocity $\boldsymbol{\omega}_p$, and angular θ are updated as

$$\mathbf{U}_p(t + \delta t) = \mathbf{U}_p(t) + \frac{\mathbf{F}_p}{M_p} \delta t, \quad (19a)$$

$$\mathbf{X}(t + \delta t) = \mathbf{X}(t) + \frac{1}{2} [\mathbf{U}_p(t + \delta t) + \mathbf{U}_p(t)] \delta t, \quad (19b)$$

$$\boldsymbol{\omega}_p(t + \delta t) = \boldsymbol{\omega}_p(t) + \frac{\mathbf{Tor}_p}{I_p} \delta t, \quad (19c)$$

$$\theta(t + \delta t) = \theta(t) + \frac{1}{2} [\boldsymbol{\omega}_p(t + \delta t) + \boldsymbol{\omega}_p(t)] \delta t. \quad (19d)$$

B. Formulation of rheological parameters

In our study, the bulk stress of a suspension is calculated through Batchelor's formulation [19,20,35]. The volume-averaged stress in a statistically homogeneous suspension is

$$\Sigma = \frac{1}{V} \int_{V_f} -p\mathbf{I} dV + \mu(\nabla\mathbf{U} + \nabla\mathbf{U}^T) + \Sigma^p, \quad (20)$$

where p is the isotropic pressure and $\nabla\mathbf{U}$ is the average velocity gradient in the fluid. Σ^p denotes the particle contribution to the bulk stress, and it is given by

$$\Sigma^p = \frac{1}{V} \sum_{n=1}^N \int_{V_p} \boldsymbol{\sigma} dV - \frac{1}{V} \int_V (\rho\mathbf{u}'\mathbf{u}')dV, \quad (21)$$

where V_p is the particle volume, $\boldsymbol{\sigma}$ is the stress, and \mathbf{u}' is the fluctuating velocity. The first term of Eq. (21) can be decomposed into two parts,

$$\int_{V_p} \boldsymbol{\sigma} dV = \int_{A_p} \frac{1}{2}(\mathbf{x}\boldsymbol{\sigma} \cdot \mathbf{n} + \boldsymbol{\sigma} \cdot \mathbf{n}\mathbf{x})dA - \int_{V_p} \frac{1}{2}(\mathbf{a}\mathbf{x} + \mathbf{x}\mathbf{a})dV, \quad (22)$$

where \mathbf{n} is the outward vector normal to the particle surface, \mathbf{x} is the displacement vector measured from the center of mass of the particle, and \mathbf{a} is the particle acceleration. \mathbf{a} is calculated as $\mathbf{a} = \mathbf{a}_p + \boldsymbol{\alpha}_p \times \mathbf{r} + \boldsymbol{\omega}_p \times \boldsymbol{\omega}_p \times \mathbf{r}$, where \mathbf{a}_p is the linear acceleration of the center of mass, and $\boldsymbol{\alpha}_p$ and $\boldsymbol{\omega}_p$ are the angular acceleration and angular velocity, respectively. Finally, the particle stress is given by

$$\Sigma^p = \frac{1}{V} \sum_{n=1}^N \mathbf{S} - \sum_{n=1}^N \mathbf{P} - \mathbf{R}, \quad (23)$$

where \mathbf{S} is the surface stress called the "stresslet" [6], \mathbf{P} is the particle acceleration stress due to particle acceleration, and \mathbf{R} is the Reynolds stress, which originates from the velocity fluctuations due to the presence of particles. These components are calculated as

$$\mathbf{S} = \int_{A_p} \frac{1}{2}(\mathbf{x}\boldsymbol{\sigma} \cdot \mathbf{n} + \boldsymbol{\sigma} \cdot \mathbf{n}\mathbf{x})dA, \quad (24a)$$

$$\mathbf{P} = \int_{V_p} \frac{1}{2}(\mathbf{a}\mathbf{x} + \mathbf{x}\mathbf{a})dV, \quad (24b)$$

$$\mathbf{R} = \frac{1}{V} \int_V (\rho\mathbf{u}'\mathbf{u}')dV. \quad (24c)$$

It should be pointed out that the calculation of \mathbf{S} contains both the hydrodynamic force and the repulsive force.

From the above formulas, the rheological properties can be calculated. The relative viscosity η_r and the first normal stress difference N_1 are defined as

$$\eta_r = 1 + \frac{\langle \Sigma_{xy}^p \rangle}{\mu\dot{\gamma}}, \quad (25)$$

$$N_1 = \langle \Sigma_{xx}^p \rangle - \langle \Sigma_{yy}^p \rangle, \quad (26)$$

where $\langle \rangle$ denotes the time-averaged quantity. In the following, N_1 is normalized by $\mu\dot{\gamma}$.

The relative viscosity can also be calculated directly from the wall shear stress (WSS):

$$\eta_r = \frac{\bar{\sigma}}{\mu\dot{\gamma}}, \quad (27)$$

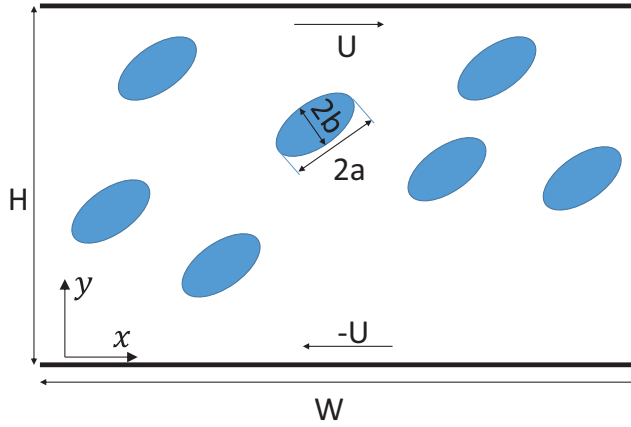


FIG. 1. Schematic diagram for elliptical particles in Couette flows. In our study, all 2D elliptical particles with different Ar have an identical area, i.e., the effective radii of all particles are identical.

where $\bar{\sigma}$ is the average shear stress and is obtained through averaging the shear stress acting on the moving flat walls over time.

C. Problem

We investigate cases of suspensions containing only one particle and multiple particles. The schematic diagram is shown in Fig. 1. There are upper and lower walls moving in opposite directions with velocity U and $-U$, respectively. For the elliptical particles, a and b are the length of semilong and semishort axes, respectively. $r_e = \sqrt{ab}$ is the effective radius of the elliptical particle. In all of the cases that we studied, r_e is identical. W and H are the length and width of the computational domain, respectively. $\dot{\gamma} = \frac{2U}{H}$ is the shear rate and μ is the viscosity of the fluid. ρ and ρ_p are densities of fluid and particles, respectively. Since only neutrally buoyant cases are considered, we have $\rho_p = \rho$.

In our study, the following key parameters are defined. The confinement ratio (β) due to the presence of walls is

$$\beta = \frac{H}{2r_e}. \quad (28)$$

The aspect ratio (Ar) of the particle is

$$Ar = \frac{a}{b}. \quad (29)$$

The Reynolds number (Re) is defined as

$$Re = \frac{\rho \dot{\gamma} r_e^2}{\mu}. \quad (30)$$

The particle concentration is defined as

$$\phi = \frac{N\pi ab}{HW}, \quad (31)$$

where N is the total number of particles.

The grid independence and time-step independence studies are performed. The results are shown in Fig. 2. In the simulated cases, the elliptical particle rotates in the shear flow with $Re = 1$, $\beta = 11$. First, dilute suspensions with only one particle are studied, as shown in Figs. 2(a) and 2(b). The

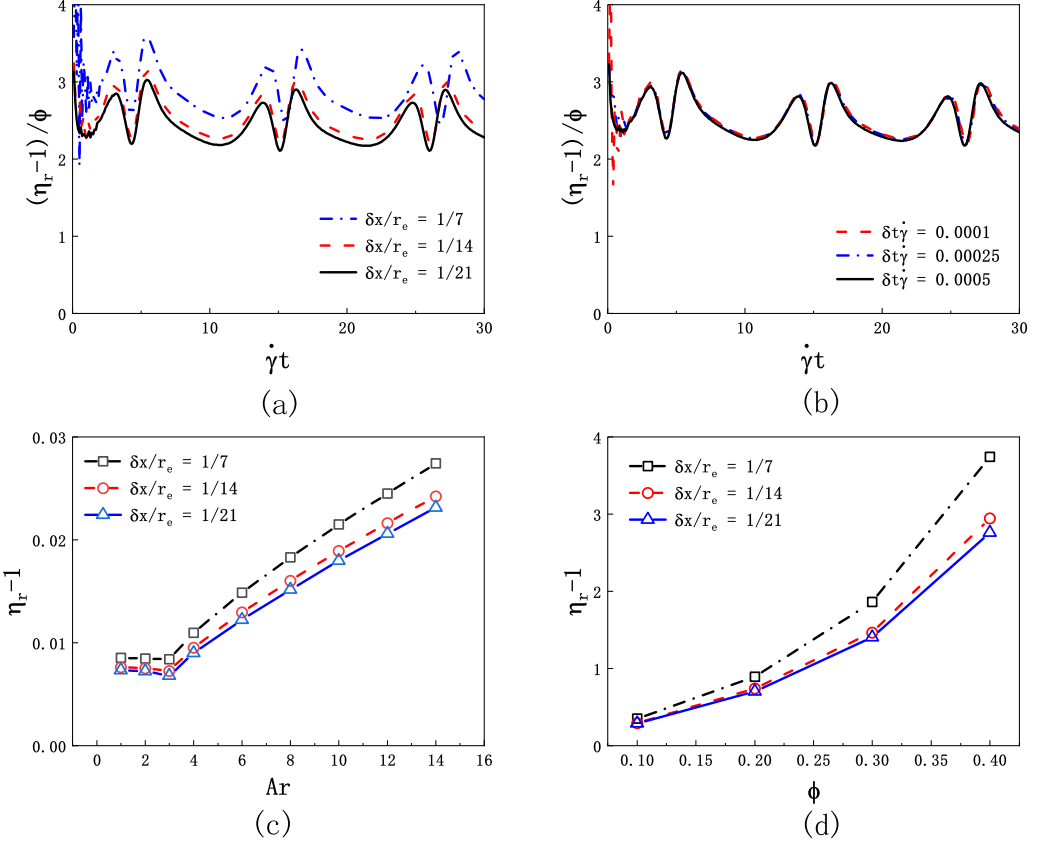


FIG. 2. Grid (a) and time-step (b) independence studies for dilute suspension containing only one particle with $Ar = 2$, $Re = 1$. (c) Grid independence studies for particles with different aspect ratios. For cases in (a), (c), a sufficiently small time step $\delta t = 0.00025 \frac{1}{\dot{\gamma}}$ is adopted and fixed. For cases in (b), a sufficient spatial resolution $\delta x = \frac{1}{14} r_e$ is adopted and fixed. In all cases, we keep a fixed Re by changing μ . (d) Grid independence study for dense cases. The average viscosity as a function of ϕ for $Ar = 2$ with different spatial resolution. Here $Re = 1$ and $\delta t = 0.00025 \frac{1}{\dot{\gamma}}$ are fixed.

average η_r for $\delta x/r_e = 1/14$ is only 4.4% higher than that of $\delta x/r_e = 1/21$. Hence $\delta x/r_e = 1/14$ seems sufficient to achieve accurate results. For time-step independence, $\delta x/r_e = 1/14$ is fixed and different $\delta t \dot{\gamma}$'s are used. It is seen that little difference is observed. Further grid independence for different Ar 's is shown in Fig. 2(c), and $\delta x/r_e = 1/14$ seems sufficient to achieve accurate results. Next, suspensions containing multiple particles are considered. Figure 2(d) shows the average relative viscosity as a function of ϕ . $\delta x/r_e = 1/14$ is also sufficient for dense suspensions considered in the paper.

Hence, in all cases, $\delta x/r_e = 1/14$ and $\delta t \dot{\gamma} = 0.0005$ are adopted for $Re = 1$, and $\delta t \dot{\gamma} = 0.0001$ is used for cases with $Re = 0.05$.

To quantify the overall orientation of suspended particles, an orientational order parameter (T_{xx}) relative to the X -axis is defined as [36]

$$T_{xx} = \frac{3}{2} n_x n_x - \frac{1}{2}, \quad (32)$$

where n_x designates the X component of the unit vector along the particle symmetry axis. $T_{xx} = 0$, 1.0, and -0.5 represent random dispersion, perfect alignment of particles with the X -axis, and alignment in the plane perpendicular to the X -axis, respectively.

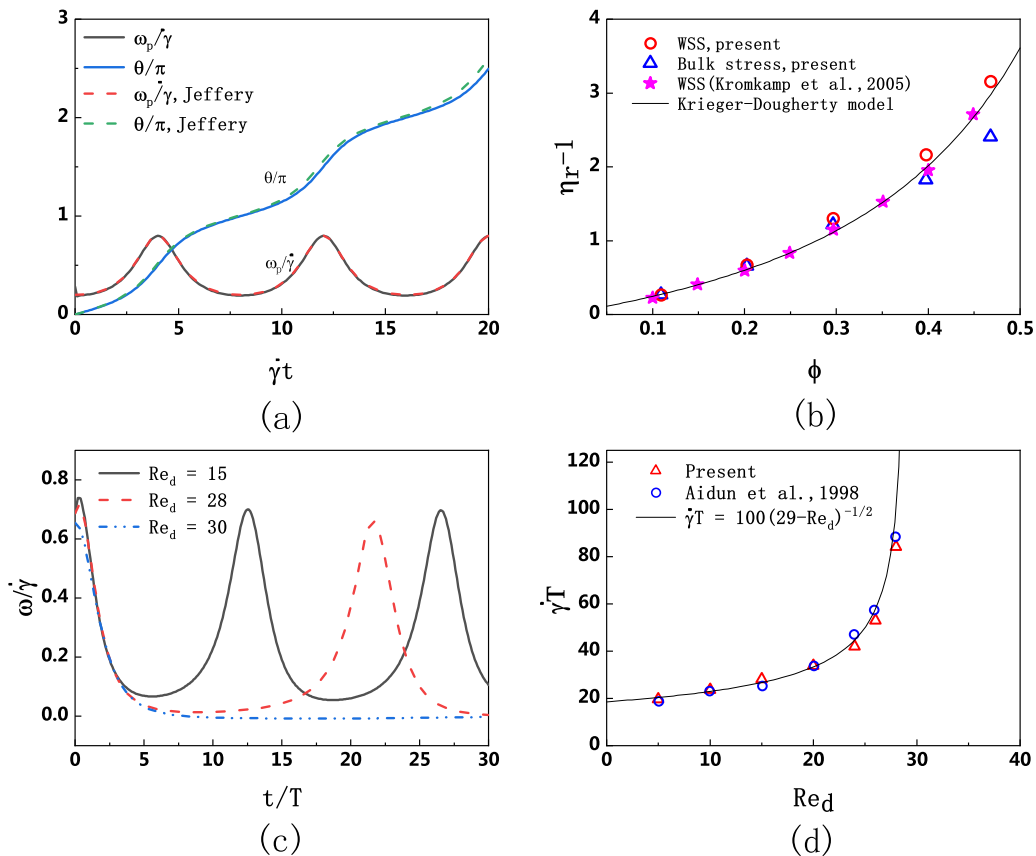


FIG. 3. (a) Orientation and angular velocity of an elliptical particle in Couette flow. The solid and dashed lines represent the simulation result at $Re = 0.08$ and Jeffery's analytical solution at $Re = 0$, respectively. (b) Relative viscosity as a function of particle concentration of circular particles. (c) The rate of change of the orientation of an elliptic particle ω at $Re = 15, 28,$ and 30 . (d) The period of the motion of the ellipse increases to infinity as Re goes to the critical value.

In all simulations, the width of the computational domain $W = 44r_e$ is fixed. Periodic boundaries are imposed at the left and right side boundaries, and the half-way bounce-back scheme is used to deal with the no-slip conditions at the upper and lower moving walls. Initially, the particles are randomly distributed in the flow. From the evolution of η_r of the suspension, we observed that in most cases, after $\dot{\gamma}t > 50$, it is converged. All simulations are generally terminated at $\dot{\gamma}t = 500$, which is sufficient to ensure convergence, and relevant properties are usually obtained after they are well-converged.

III. VALIDATION

Three tests are performed to validate our computational code. The first is an elliptical particle with $Ar = 2$ rotating in shear flow. In the simulation, the key parameters are $a = 10lu$, $\dot{\gamma} = 0.0005ts^{-1}$, $Re = 0.08$, $W = 12a$, and $H = 10a$. Here lu and ts are the lattice units. $a = 10lu$ means a is discretized by 10 grids and $\dot{\gamma} = 0.0005ts^{-1}$ means $1/\dot{\gamma}$ is discretized into $1/0.0005 = 2000$ steps. The orientation angle (θ) of the particle is defined as the angle between its long axis and the X-axis. The orientation angle and angular velocity (ω_p) as functions of time are shown in Fig. 3(a). It is seen that our results are consistent with Jeffery's analytical solution [5].

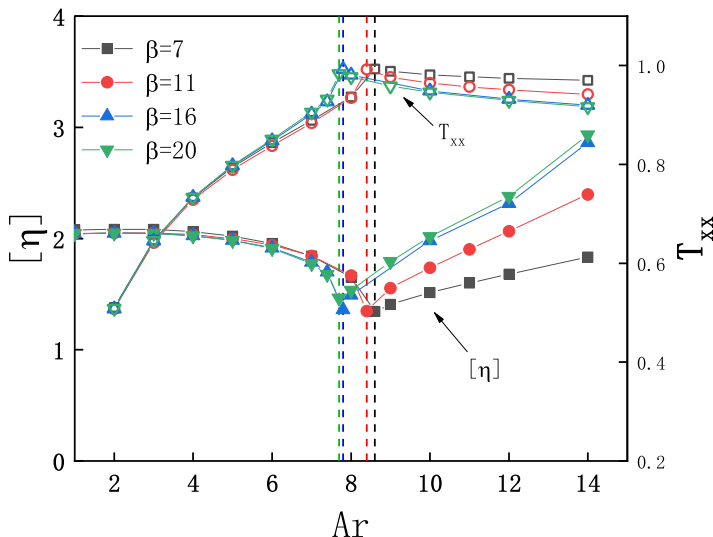


FIG. 4. The intrinsic viscosity $[\eta]$ and orientational order parameter T_{xx} as functions of Ar with different β 's. The solid and hollow symbols correspond to the values of $[\eta]$ and T_{xx} , respectively. The vertical dashed lines are drawn to denote the critical Ar , i.e., Ar_c , specifically $Ar_c \approx 8.6, 8.4, 7.8,$ and 7.7 for $\beta = 7, 11, 16,$ and 20 , respectively. For these cases, $Re = 0.1$ is fixed.

The second case is multiple circular particles moving in the shear flow. In the simulation, $a = 20lu$, $\dot{\gamma} = 0.000025t s^{-1}$, and $Re = 0.02$. The relative viscosity of the suspensions is shown in Fig. 3(b). Our results are consistent with those of the analytical Krieger-Dougherty model [8] and those in [34]. It is noted that the results obtained from bulk stress based on Batchelor's formulation are lower than those based on the wall shear stress at high particle concentration. This point has also been observed in Ref. [22].

We further perform simulation of an elliptical particle with $Ar = 2$ rotating in the shear flow. In these simulations, $W = 40a$, $H = 10a$, $\dot{\gamma} = 0.0002$, $a = 12lu$. The Reynolds number is $Re_d = 4\rho\dot{\gamma}a^2/\mu$. Figures 3(c) and 3(d) show the results. From Fig. 3(c) we can see that as Re increases, e.g., from $Re = 15$ to 28 , the rotational period ($\dot{\gamma}T$) increases. When $Re = 30$, the rotation-induced arrest occurs. Figure 3(d) shows the variation trend of period. As Re_d goes to the critical value, which is approximately 29 , the period increases to infinity. Therefore, our results agree well with those in Ref. [30].

IV. RESULTS AND DISCUSSION

A. Dilute suspension with one particle

First dilute suspensions with one particle were investigated. One particle in a periodic computational domain has been widely used to study the orientation dynamics and rheology of particles [19,23–25].

First, cases with different confinement ratio β with $Re = 0.1$ are examined. Figure 4 shows the intrinsic viscosity $[\eta] = (\eta_r - 1)/\phi$ and T_{xx} as functions of Ar . For different β , the intrinsic viscosity exhibits a similar variation with Ar , and the variation of η_r is highly related to T_{xx} . As shown in Fig. 4, the position of the critical aspect ratio is the same for both $[\eta]$ and T_{xx} . With the increase of β , the convergence is clearly observed and $\beta = 16$ is close to the domain-size independent case. In the following, $\beta = 16$ is fixed and parameter ranges $Ar \in [1, 14]$, $Re \in [0.05, 1]$.

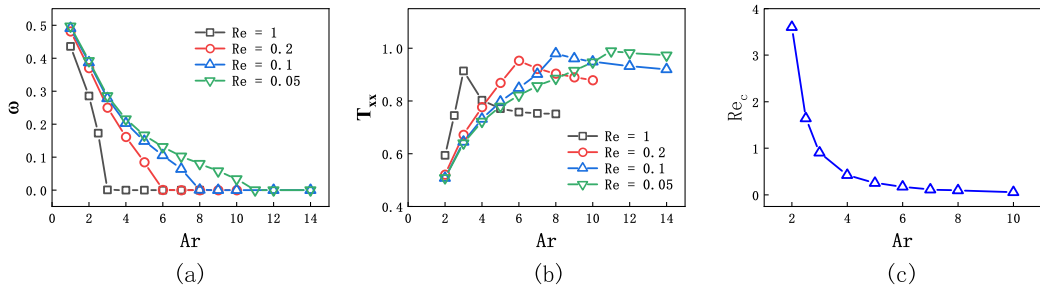


FIG. 5. (a) Time-averaged angular velocity ω_p of a particle as a function of aspect ratio Ar for different Re. (b) Orientational order parameter (T_{xx}) as a function of Ar for different Re. (c) Critical Reynolds number Re_c as a function of Ar. $\beta = 16$ is fixed.

1. Rotation motion of the particle

We first investigate the rotation state of an elliptical particle in a wall-bounded Couette flow. An elliptical particle or ellipsoid can change from a time-periodic to a steady state due to the inertia effect, and this was identified by Aidun *et al.* [30] for the first time. Figure 5(a) shows the time-averaged angular velocity ω_p . For a specific Re, ω_p decreases with the increase of Ar, and rotation arrest ($\omega_p = 0$) occurs at a critical aspect ratio Ar_c . With the increase of Re, the critical aspect ratio decreases, e.g., $Ar_c \approx 8$ for Re = 0.1 and $Ar_c \approx 6$ for Re = 0.2.

On the other hand, for a particle with a specific Ar, rotation arrest occurs at a critical aspect ratio Re_c . Figure 5(c) shows the critical Reynolds number Re_c as a function of Ar, and a decrease of Re_c is observed with the increase of Ar. The results are consistent with the previous studies, including 3D simulations and analytical study. Rosen *et al.* [25] show that a neutrally buoyant prolate spheroid with Ar = 2 stops rotating at $Re_c \approx 59.4$, while it stops at $Re_c \approx 5.58$ for Ar = 4. Using a generalization of reciprocal theorem, Subramanian and Koch [15] show that the fiber ceases to rotate above a critical Reynolds number Re_c , and Re_c turns out to be $O(\ln(Ar)/Ar)$, i.e., Re_c decreases with the increase of Ar.

Figure 5(b) shows the orientational order parameter T_{xx} as a function of Ar for different Re. T_{xx} first increases with the increase of Ar. A higher value of T_{xx} means particles align more with the flow direction, i.e., a lower angle between the particle major axis and the flow direction. That can be understood in the following way. For an elliptical particle rotating in shear flows, the angular velocity reaches its peak and valley when the particle is normal and aligned to the flow (the X-axis), respectively. However, the peak and valley periods are different. Usually the valley period is significantly longer than the peak period [see Fig. 3(a)]. Generally speaking, during one rotating period, the valley period of a slender rodlike particle (higher Ar) is much longer. Therefore overall, the slender rodlike particle seems more aligned with the flow. In other words, T_{xx} would increase with Ar and be closer to unity.

When $Ar > Ar_c$, the particle's motion mode changes from tumbling to a steady inclined state, and decreases of T_{xx} are observed with increasing Ar. Under this circumstance, the orientation angle between the particle long axis and the flow direction increases with the increase of Ar. Hence the particle becomes less aligned with the flow, and T_{xx} decreases with increasing Ar in this stage.

2. Rheological properties

Next, we investigate the rheological properties of dilute suspension with one particle, and we discuss the relation between the rheology and the particle rotational motion.

Figure 6(a) shows the relative viscosity as a function of Ar for different Re. The reverse variation is observed when compared to T_{xx} , as shown in Fig. 5(b). In the first stage, the particles rotate in the flow and η_r decreases with the increase of Ar. In the second stage, particle rotation arrest

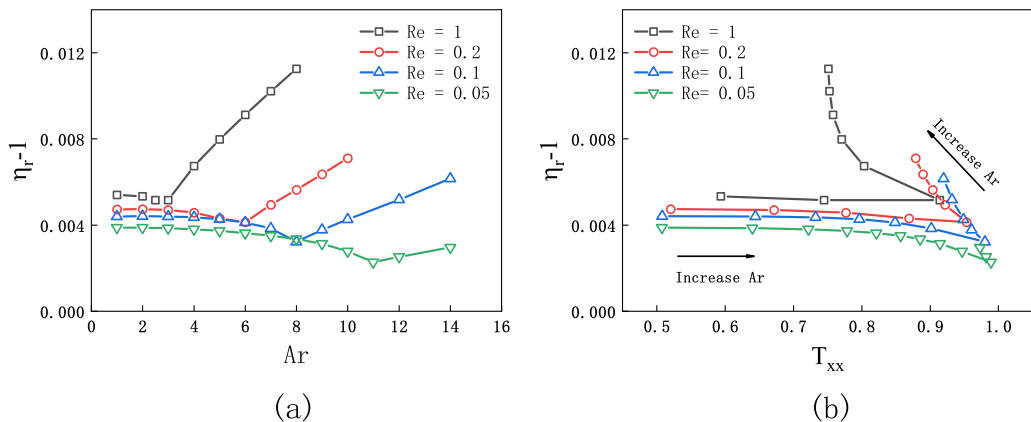


FIG. 6. The relative viscosity as a function of (a) Ar and (b) T_{xx} for different Reynolds number. The black arrows denote the direction of increasing Ar . $\beta = 16$ is fixed.

occurs and η_r increases with Ar . The transition of η_r is highly correlated to the particle's rotational motion. Figure 6(b) shows η_r as a function of T_{xx} . Minimum viscosity is observed corresponding to maximum T_{xx} (maximum particle alignment) for all Reynolds numbers considered here.

Here we can explain the results in Fig. 6 in the following way. In the first stage, with the increase of Ar , the particle becomes more aligned with the flow, and disturbance on the flow due to the presence of the particle is weaker. Hence η_r decreases slightly. In the second stage, particles remain stationary and inclined in the flow. With the increase of Ar , the particle becomes less aligned with the flow, i.e., T_{xx} decreases, and due to the increased disturbance, η_r increases. However, the increase in viscosity does not necessarily require the alignment to decrease. With the increase of Ar , the Reynolds number based on the particle's major axis increases, and this can lead to an increase of viscosity known as shear thickening. As shown in Fig. 6(b), a stronger increase of viscosity for higher Re is observed, and for $Re = 1$, the alignment curve becomes nearly vertical, i.e., the viscosity continues to increase with Ar , though T_{xx} is almost constant.

Further, the contributions of stresslet (S), particle acceleration (P), and Reynolds stress (R) in the rheology are analyzed. Figure 7 shows the contributions of S , P , and R in the rheology at different Re . For lower Reynolds number ($Re = 0.05$), the inertial effect is negligible. The contribution of S is dominant for both η_r and N_1 . The values of P and R are nearly zero and can be neglected. In addition, a negative to positive change is observed for N_1 with the increase of Ar . For higher Reynolds number ($Re = 1$), the inertial effect is apparent for both η_r and N_1 . The contribution of R in η_r is small, but the value of R increases with the increase of Ar . For N_1 , the contributions of both S and R are important and increase with the increase of Ar . For both Reynolds numbers considered here, the contribution of P in rheology is negligible.

B. Microstructure and rheological properties of dense suspensions

In this section, the microstructure and rheological properties of dense suspensions with many particles are investigated. Here $\beta = 11$ is fixed, and the effects of Ar , Re , and ϕ are discussed in detail. In this section, parameter ranges $Ar \in [1, 8]$, $Re \in [0.05, 1]$, and $\phi \in [0.1, 0.4]$.

1. Particle distribution

First the cases of $Ar = 1, 2$, and 8 are considered. Figure 8 shows instantaneous particle distributions and contours of x -component velocity at $\phi = 0.4$. For circular particles ($Ar = 1$), there are layers of particles close to the channel walls [see Fig. 8(a)]. In cases with higher Re and Ar , particles' distribution becomes more homogeneous. Figures 8(c), 8(f) and 8(i) show the average U_x

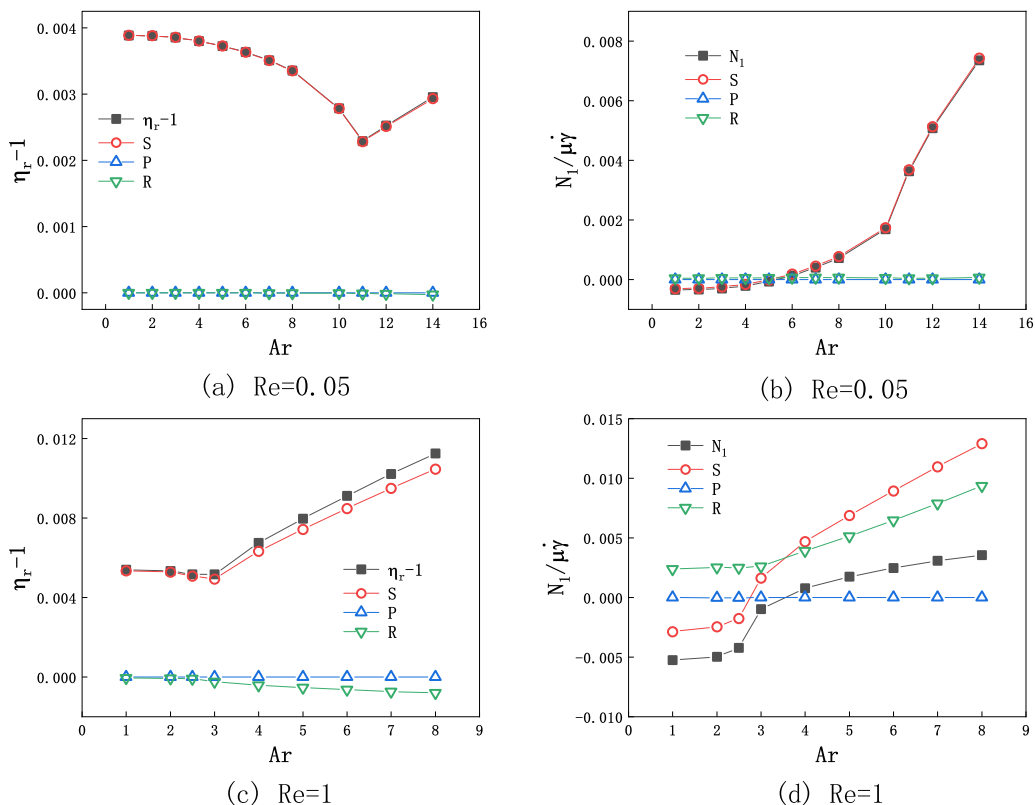


FIG. 7. Relative viscosity (a), (c) and first normal stress difference (b), (d) as functions of Ar for $Re = 0.05$ [(a) and (b)] and $Re = 1$ [(c) and (d)]. The corresponding contributions of stresslet (S), particle acceleration (P), and Reynolds stress (R) are shown as well. $\beta = 16$ is fixed.

along the Y -axis. It is seen that in the cases with higher Re or Ar , the discrepancies between the actual velocity profile and that without particles are more significant. That partially demonstrates the stronger disturbance of the particles to the fluid.

To quantitatively describe the spatial distribution of the particles, the local particle concentration (ϕ_y) is adopted [10],

$$\phi_y = \frac{1}{W} \left\langle \int \chi(\mathbf{x}) dx \right\rangle, \quad (33)$$

where $\langle \cdot \rangle$ represents the time average and $\chi(\mathbf{x})$ is an indicator function. $\chi(\mathbf{x})$ is defined as

$$\chi(\mathbf{x}) = \begin{cases} 1, & \mathbf{x} = \mathbf{x}_s, \\ 0, & \mathbf{x} = \mathbf{x}_f, \end{cases} \quad (34)$$

where \mathbf{x}_s and \mathbf{x}_f represent the location \mathbf{x} inside and outside of particles.

Figures 9(a)–9(c) shows the profiles of the local particle concentration (ϕ_y) for different ϕ at $Re = 0.05$ and 1. Due to the symmetry of the system, only half of the channel is considered. It is seen that generally, the particles are evenly distributed in the central region but become fewer and fewer in the region close to the wall. However, for circular particles, in the very dense case at low Re , e.g., $\phi = 40\%$ at $Re = 0.05$, ϕ_y may increase dramatically in the region close to the wall [see Fig. 9(a)]. There is a local peak near the wall region, and particle layering is observed. That is consistent with what we have seen in Fig. 8(a). It is noted that the structured particle layering in

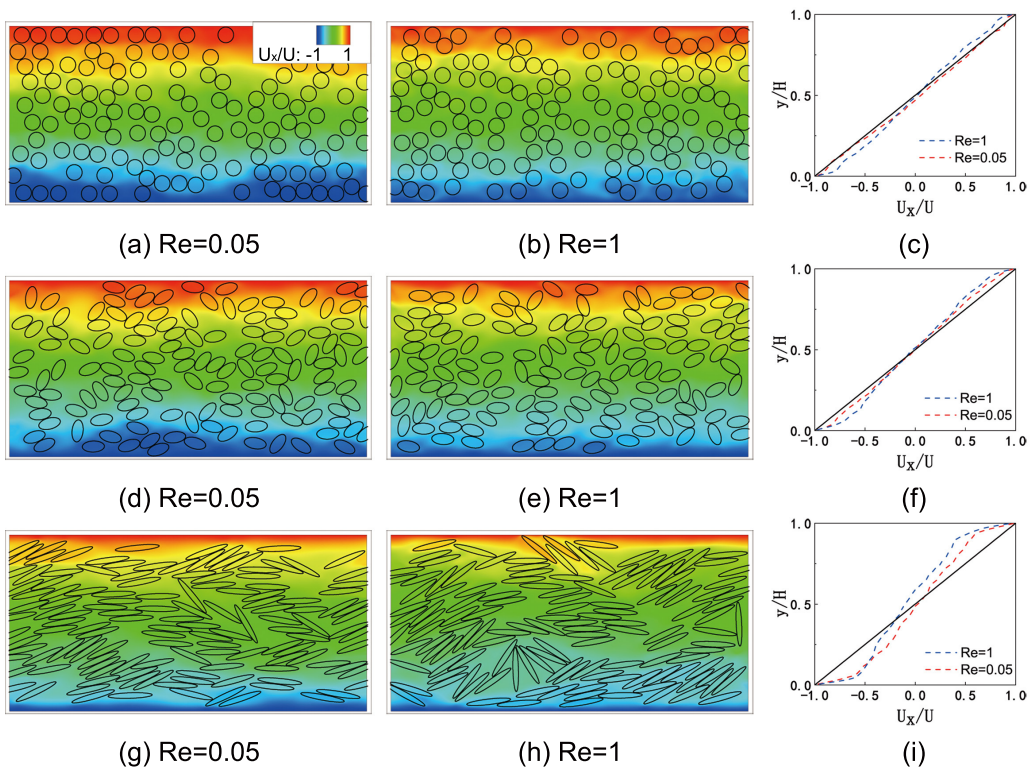


FIG. 8. The instantaneous particle distributions and contours of x -component velocity (U_x) for (a), (d), (g) the cases of $Re = 0.05$, and (b), (e), (h) the cases of $Re = 1$. The upper, middle, and lower rows correspond to cases of $Ar = 1, 2$, and 8 , respectively. (c), (f), (i) Time-averaged U_x along the Y -axis. The black solid line represents the undisturbed shear flow without particles. In these cases, $\beta = 11$ and $\phi = 0.4$ are fixed.

wall-bounded suspensions has been reported in the earlier simulations [10,22] and experiments [12] of spherical particle suspensions.

Shear-induced diffusion caused by hydrodynamic particle-particle interaction plays a key role in the dynamic behavior of non-Brownian suspensions at the limit of negligible inertia [29,37]. Due to the shear-induced diffusion, particles can move apart from their original streamlines and toward the boundary wall. Near a flat wall, a balance between the wall repulsive force and particle-particle interaction force causes the particles to move along the flow direction, and they are trapped near the wall. Hence particle layering is observed. For the elliptical particles, the particle layering is weak for both $Re = 0.05$ and 1 . This may be caused by particle rotation. As an elliptical particle rotates near the wall, the direction of the particle-wall force changes with time. Hence for elliptical particles, it is difficult to move along the streamline near the wall even at a small Re .

In Figs. 9(a)–9(c), we can also see that regardless of ϕ and Ar , the spatial distribution of particles is more biased toward the centerline at the higher Re . The concentrated profile is governed by a competition between inertial migration and shear-induced diffusion. The inertial migration would cause a single particle, certainly a sphere, to move towards the centerline in plane Couette flow, while the shear-induced diffusion causes the particles to move apart from their original streamlines. At higher Re , inertial migration is dominated and particles tend to concentrate close to the centerline.

Figure 9(d) shows T_{xx} as a function of ϕ . For small Ar ($Ar = 2$), T_{xx} increases with the increase of ϕ , i.e., particles align more in the flow direction for higher particle concentration. For large Ar ($Ar = 5, 8$), a small variation of T_{xx} is observed for different ϕ . The saturation of T_{xx} for large Ar

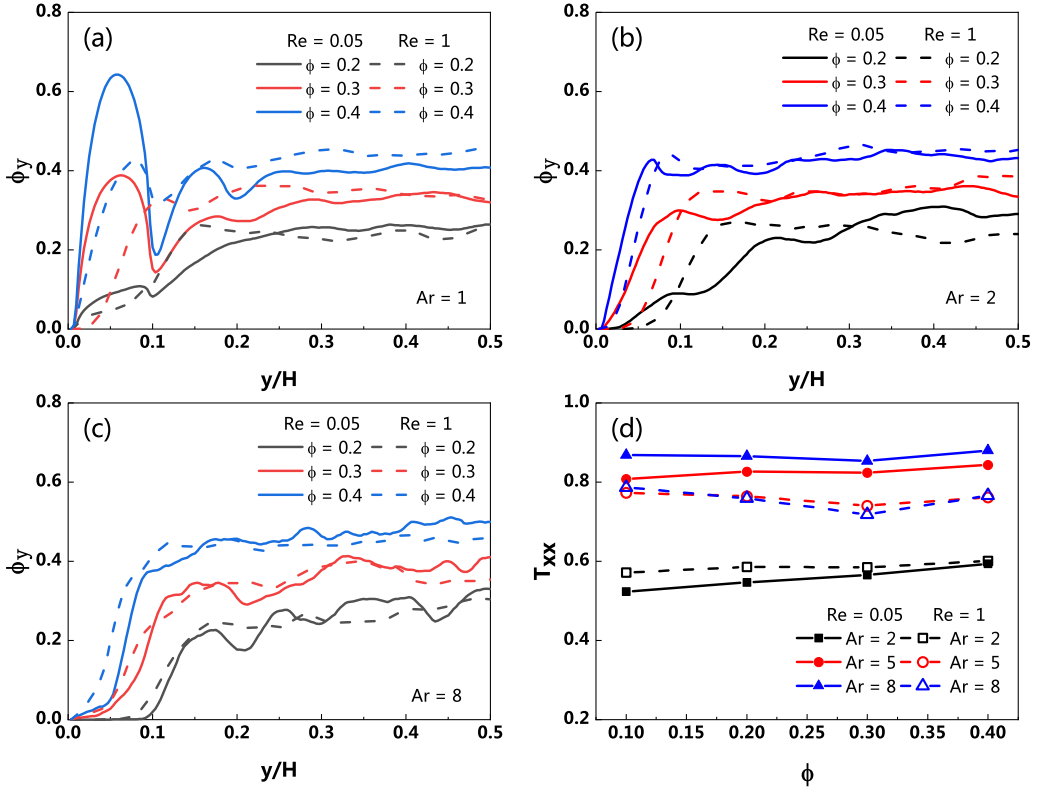


FIG. 9. The concentration profiles (particle distributions) in the cases of (a) $Ar = 1$, (b) $Ar = 2$, and (c) $Ar = 8$ with different ϕ at $Re = 0.05$ and 1. The solid lines and dashed lines correspond to $Re = 0.05$ and 1, respectively. (d) T_{xx} as a function of ϕ for different Re and Ar .

can be understood in the following way. For an elliptical particle rotating in shear flows, the angular velocity reaches its peak and valley when the particle is normal and aligned to the flow, respectively. However, the peak and valley period is different. Usually, the valley period is significantly longer than the peak period. Hence particles align to the flow with a higher probability than normal to the flow. When multiple particles are considered, the constraint of the near particle causes a particle to keep its orientation. Thus a longer valley period can be observed with the increase of ϕ . So the valley period is dominant gradually with the increase of ϕ .

For $Ar = 2$, at low ϕ , both the peak and valley period contribute to the value of T_{xx} . With increasing ϕ , the valley period contributes more, so T_{xx} increases with ϕ . However, for high Ar , e.g., $Ar = 8$, the value of T_{xx} mainly depends on the valley period even at the low ϕ . So a very small change of T_{xx} is observed with ϕ for high Ar , i.e., the values of T_{xx} seem to reach saturation.

2. Rheological properties

In this section, the rheological properties will be discussed in detail. Figure 10(a) shows η_r as a function of ϕ for different Ar and Re . It is seen that η_r increases with the increase of ϕ for different Ar . In addition, η_r increases with Re , i.e., shear thickening with Re is observed. The thickening is more significant as ϕ increases. The results are consistent with the results of circular and spherical particle suspension simulations [22,29].

Another key rheological property, the first normal stress difference will also be discussed. Figure 10(b) shows N_1 as a function of ϕ for the cases with different Ar at $Re = 0.05$ and 1. At

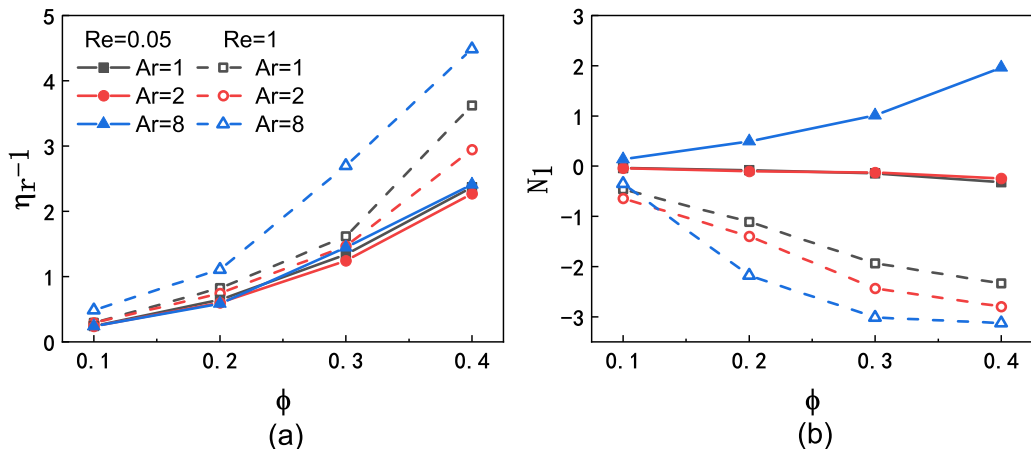


FIG. 10. The relative viscosity (a) and first normal stress difference (b) as functions of ϕ for different Ar and Re .

finite Re , theoretical studies have shown that N_1 of spherical particle suspensions is negative, and the second normal stress difference is positive in the limit of $\phi \rightarrow 0$ and $Re \ll 1$ [13,14]. In this study, Fig. 10(b) shows that for a circular particle suspension, N_1 is negative in the range of ϕ and Re considered here, and $|N_1|$ increases with ϕ and Re . That is consistent with the numerical results of sphere suspensions [20,22].

For cases of $Ar = 2$, the situation is similar to that of $Ar = 1$. However, for $Ar = 8$, N_1 is positive and negative for $Re = 0.05$ and 1, respectively. This is due to the contribution of the positive stresslet in N_1 [11], and details will be explained in the later in the paper.

Next, we would like to focus on the Ar effect on η_r and N_1 . The cases with different Ar but identical $\phi = 0.3$ are simulated. The results including T_{xx} are presented in Fig. 11. For both $Re = 0.05$ and 1, with the increase of Ar , η_r first decreases and then increases, i.e., there is a valley in the curve. For the overall orientation of the particles, T_{xx} increases with Ar and becomes closer to unity. In other words, the particles are more aligned with the flow as Ar increases. But when the aspect ratio is greater than a threshold Ar_t , T_{xx} remains almost unchanged. Here $Ar_t \approx 4$ for $Re = 0.05$ and $Ar_t \approx 3$ for $Re = 1$. It seems that the particle alignment is limited by the particle-particle interaction for $Ar > Ar_t$. Besides, at a higher Re , particle-particle interaction becomes stronger so lower Ar_t is observed.

When the particles are more aligned with the flow, particle-flow interaction or the particle disturbance on the flow is weak. Therefore, η_r would decrease first. When $Ar > Ar_t$, even T_{xx} is almost a constant, but more slender particles (higher Ar) have stronger particle-particle interactions [19], which increases η_r . The inertial effect on η_r can be seen from a comparison between Figs. 11(a) and 11(c). At a specific Ar , η_r at $Re = 1$ seems significantly larger than that at $Re = 0.05$, especially when Ar is large. Generally, the inertia enhances the particles' disturbance on the flow [see also Figs. 8(c), 8(f) and 8(i)].

The first normal stress N_1 increases with Ar monotonously from negative to positive values at low Re . At high Re , N_1 is always negative and it decreases with Ar slightly. This can be understood through the contribution of different stress mechanisms defined in Eq. (23).

As shown in Fig. 11, the contribution of S on η_r is dominant while those of the P and R terms are negligible for all cases of $Re = 0.05$ and 1. For N_1 , at $Re = 0.05$, from Fig. 11(b) we can see that the contribution of S is dominant and the contribution of P can be neglected. When Ar is small, the contribution of R is also negligible, but with the increase of Ar , R increases monotonously and it begins to contribute to N_1 . At $Re = 1$, Fig. 11(d) shows that the contribution of R is more prominent than that of S , and the contribution of P can be neglected. Meanwhile, the contribution of S may be

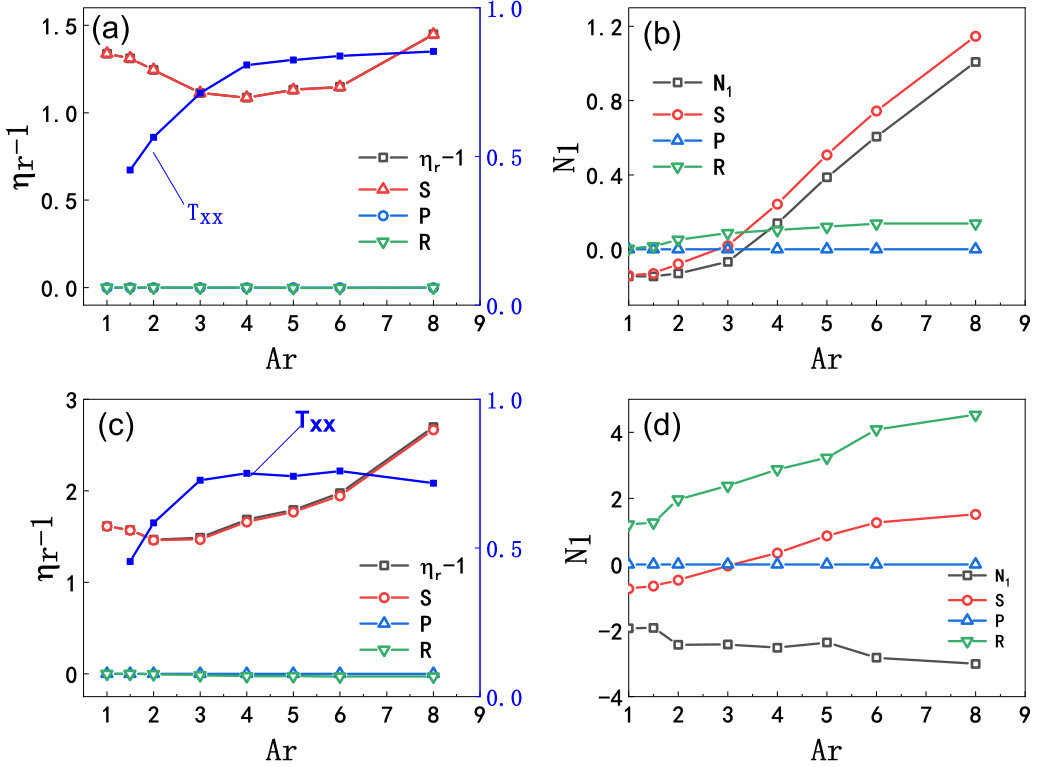


FIG. 11. (a), (c) Relative viscosity and (b), (d) first normal stress difference as functions of Ar at (a), (b) $Re = 0.05$ and (c), (d) $Re = 1$. The corresponding contributions of stresslet (S), particle acceleration (P), and Reynolds stress (R) are shown as well. The values of T_{xx} (blue solid lines) in (a) and (c) are labeled on the right-hand side of the figure. In these cases, $\phi = 0.3$ is fixed.

negative ($Ar < 3$) or positive ($Ar > 3$). It is noted that a positive R leads to a negative N_1 [Eq. (23)]. Hence, N_1 at $Re = 1$ is generally negative.

Here we can explain the results of N_1 for different Ar in Fig. 10(b). For $Re = 0.05$, the value of N_1 depends on the contribution stresslet. For $Ar = 1$ and 2, the contribution of S in N_1 is positive, and for $Ar = 8$, a negative contribution of S is observed as shown in Fig. 11(b). Hence positive N_1 is observed for $Ar = 8$ in Fig. 10(b). For $Re = 1$, the negative N_1 for $Ar = 1$ and 2 is the result of negative S and positive R , while for $Ar = 8$ the negative N_1 is caused by the large positive value of R .

3. Statistics of velocity fluctuations

One small suspended particle in shear flow may move with the flow almost without disturbance. However, many particles' migration in suspensions would significantly depart from the streamline due to the particle-particle interaction [22]. To have a better understanding of particle suspension, the statistical physics of particle fluctuation is presented. In the following, the probability density function (PDF) of linear lateral velocity (U_y) and angular velocity (ω_p) is analyzed. Here particles near the wall are not considered to minimize wall effects. $\dot{\gamma}H/2$ and $\dot{\gamma}$ are used to normalize U_y and ω_p , respectively.

Figures 12 and 13 show the PDF for U_y and ω_p for different ϕ , Re , and Ar , respectively. For sphere suspensions, the PDF of velocity fits a general form [22,38]

$$P \propto \exp[-c|U|^d], \quad (35)$$

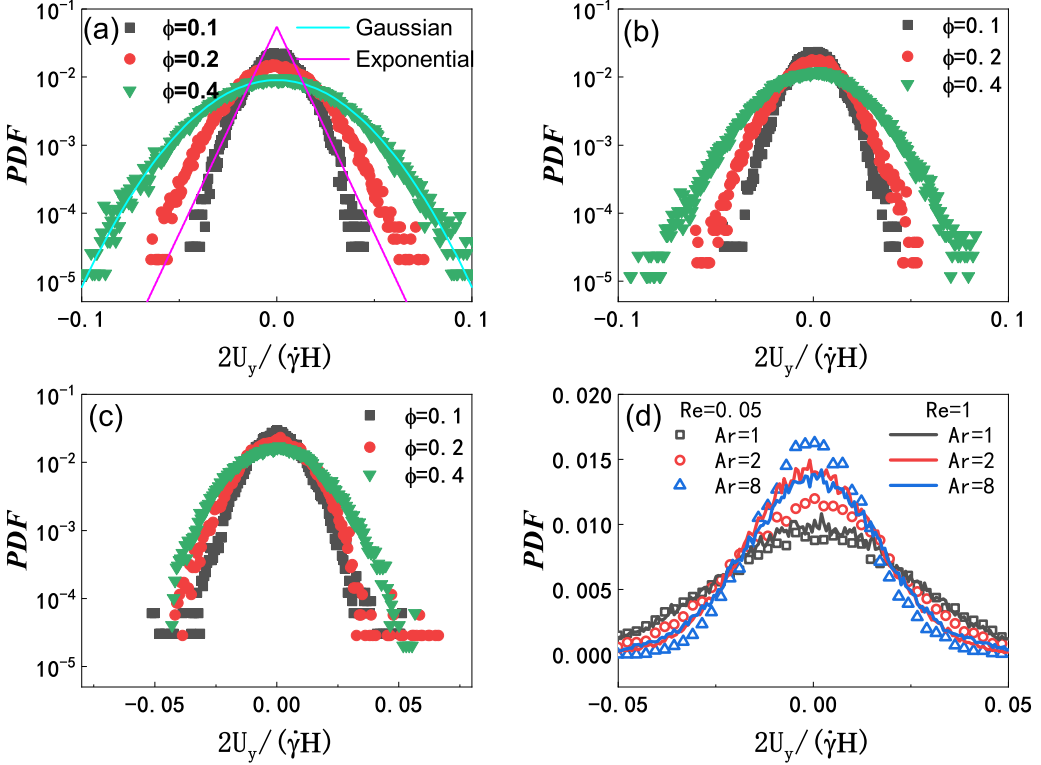


FIG. 12. The probability density function of U_y at $Re = 0.05$ for different ϕ for (a) $Ar = 1$, (b) $Ar = 2$, and (c) $Ar = 8$. (d) PDF(U_y)'s for different Ar and Re in the cases of $\phi = 0.4$.

where c is a fitting parameter. $d = 1$ and 2 correspond to exponential and Gaussian distributions, respectively. Generally, an exponential distribution qualitatively describes dilute cases well, and a Gaussian distribution works well for dense cases. Meanwhile, an intermediate d between 1 and 2 represents a transition from an exponential distribution to a Gaussian distribution when ϕ is moderate. In Fig. 12(a), the fitting results for $\phi = 0.1$ with an exponential distribution and $\phi = 0.4$ with a Gaussian distribution seem quite perfect. Our results also show that with the increase of ϕ , the width of the PDF increases and the peak value decreases for all Ar simulated here.

With the increase of Ar , the peak values increase and the width decreases. As Ar increases, particles become more aligned with the flow direction, which limits the lateral movement, therefore $U_y = 0$ has a higher probability to appear. For the inertial effect, from Fig. 12(d), we can see that when $Ar = 2$, the PDF peaks of $Re = 1$ are higher than those of $Re = 0.05$. However, for $Ar = 8$, the situation is different. The PDF peaks of $Re = 1$ are lower than those of $Re = 0.05$ because the particles are slightly less aligned with the flow direction at $Re = 1$ [a smaller T_{xx} ; see Figs. 11(a) and 11(c)].

We would like to further discuss the PDF of ω_p . As shown in Fig. 13, for $Ar = 1$, the PDFs of ω_p are not so symmetric, especially at lower ϕ , e.g., $\phi = 0.1$ and the peaks appear at $\omega_p \approx 0.5\dot{\gamma}$. With the increase of ϕ , the peak value decreases and the width of the PDF increases. The average ω_p increases with ϕ . For $Ar = 2$, the situation is similar to that of $Ar = 1$ but the curves become flatter and the peak values appear at a smaller ω_p . For $Ar = 8$, the distribution looks very symmetric and the peaks appear at $\omega_p \approx 0$. With the increase of ϕ , the corresponding peak value decreases. For the inertial effect, Fig. 13(d) shows the PDFs of ω_p at $Re = 1$ and 0.05 for cases with $\phi = 0.4$. For $Ar = 1$ and 2 , the peak value appears at a lower ω_p at higher Re . For $Ar = 8$, the peak value decreases slightly with the increase of Re .

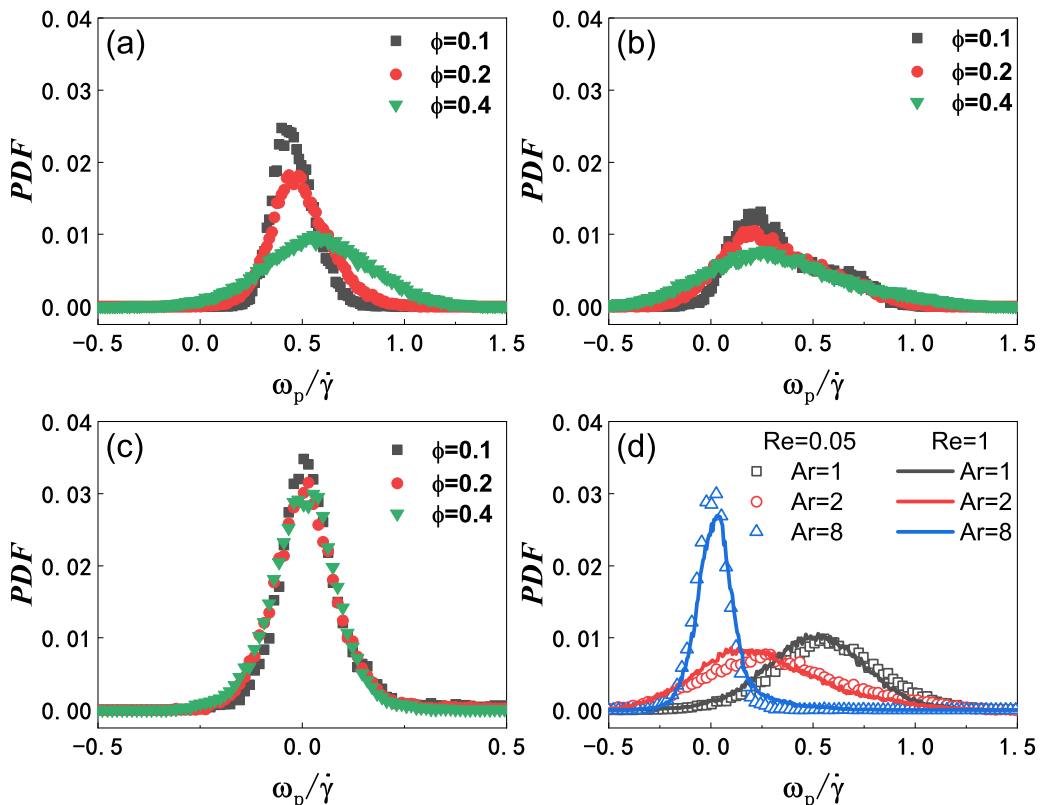


FIG. 13. The probability density function of ω_p at $Re = 0.05$ for different ϕ for (a) $Ar = 1$, (b) $Ar = 2$, and (c) $Ar = 8$. (d) PDFs of ω_p for different Ar and Re in the cases of $\phi = 0.4$.

V. CONCLUSION AND FUTURE WORK

In this work, we studied the microstructure and rheological properties of neutrally buoyant elliptical particles in Couette flow using the immersed boundary lattice Boltzmann method. The effects of particle aspect ratio (Ar), fluid inertia (Re), and particle concentration ϕ on the rheological properties of dilute and dense suspensions are investigated in detail.

For suspensions containing only one single particle, the effects of Re and Ar on the particle rotational motion and the rheological properties are investigated. For any finite Re considered in the paper, particle rotates periodically in the shear flow for $Ar < Ar_c$. The critical aspect ratio Ar_c decreases with the increase of Re . Particles with $Ar > Ar_c$ cease to rotate and keep in a steady-inclined state. Corresponding to the rotational state, the orientational order parameter T_{xx} increases with the increase of Ar and then decreases with Ar when rotation arrest occurs. Particles with higher values of T_{xx} align more in the flow direction. Hence with the increase of Ar , the particles are more aligned with the flow for $Ar < Ar_c$ and less aligned with the flow for $Ar > Ar_c$. Meanwhile, the variation of the particle rotational motion from tumbling to a steady state induces a nonmonotonic variation of viscosity. The viscosity correlates with the particle alignment and the minimum viscosity corresponding to the maximum alignment. Our results show that the change of particle rotational motion and viscosity for any finite Re considered here is similar, i.e., for any Re , an elliptical particle ceases to rotate at a critical aspect ratio Ar_c and induces a non-monotonic variation of viscosity. The value of Ar_c depends on Re and decreases with the increase of Re .

For suspensions containing multiple particles, the effects of particle aspect ratio and Re on the particle distribution and particle orientation are investigated. At low Re , circular particles ($Ar = 1$) accumulate near the wall, and wall-induced particle layering is observed. However, the particle distribution is more biased toward the midplane due to the inertial migration at high Re . For elliptical particles, particle layering is not observed. With a specific particle concentration, e.g., $\phi = 0.3$, T_{xx} increases with Ar and T_{xx} remains almost unchanged when the aspect ratio is greater than a threshold $Ar > Ar_t$. The value of the threshold Ar_t is smaller for higher Re . With the increase of Ar , the relative viscosity first decreases due to particle alignment but increases due to high particle-particle interaction.

The contributions of stresslet, particle acceleration stress, and Reynolds stress [6] on η_r and N_1 are analyzed. The contribution of stresslet is dominant, and those of particle acceleration stress and Reynolds stress in η_r are negligible for different Ar , ϕ , and Re considered here. As for N_1 , a negative to positive change of stresslet contribution is observed with the increase of Ar . Besides the major contribution of stresslet, the Reynolds stress also contributes significantly to N_1 and becomes more important in cases with higher Ar and Re .

We also investigated the microstructure and the particle velocity fluctuations statistically. For circular particles ($Ar = 1$) at $Re = 0.05$, structured particle layering is dominant in the wall region, and homogeneous structure is observed near the center of the channel. With the increase of Re , the concentration of circular particles near the wall decreases. However, for elliptical particles, there is no structured particle layering near the wall, and the suspensions become more homogeneous for higher Ar . Similar to the sphere suspensions [22,38], $PDF(U_y)$ of particles with different Ar all exhibit exponential distributions in dilute cases and Gaussian distributions in dense cases. The distribution of the angular velocity of particles was also obtained. For circular particles ($Ar = 1$), the average values of ω_p are roughly equivalent to $0.5\dot{\gamma}$, and ω_p for higher Ar is lower.

Our studies provide the fundamental knowledge of elliptical particle suspensions in Couette flow. However, our study is limited to elliptic particles, which can only tumble (including rotation arrest) in two dimensions. In three dimensions, spheroids can spin, tumble, or precess. The subtle nature of the rheology may arise from a tumbling-spinning transition that occurs for thin oblate spheroids [16], and there cannot be an analog of this in two dimensions. Anyway, tumbling is a very common motion mode for 3D spheroidal particles in shear flows. Qualitative results of 2D simulations obtained here are a stepping stone to investigate 3D spheroid suspensions in Couette flow. To gain a better understanding of the nonspherical suspensions, we plan to perform 3D simulations of both prolate and oblate particle suspensions in the near future.

ACKNOWLEDGMENT

This work was supported by Natural Science Foundation of China (NSFC) Grants No. 11972342, No. 11772326, and No. 11621202.

-
- [1] C. K. Aidun and Y. Lu, Lattice Boltzmann simulation of solid particles suspended in fluid, *J. Stat. Phys.* **81**, 49 (1995).
 - [2] J. J. Stickel and R. L. Powell, Fluid mechanics and rheology of dense suspensions, *Annu. Rev. Fluid Mech.* **37**, 129 (2005).
 - [3] S. Mueller, E. Llewellyn, and H. Mader, The rheology of suspensions of solid particles, *Proc. R. Soc. A* **466**, 1201 (2010).
 - [4] A. Einstein, Eine neue bestimmung der moleküldimensionen, *Ann. Phys.* **324**, 289 (1906).
 - [5] G. B. Jeffery, The motion of ellipsoidal particles immersed in a viscous fluid, *Proc. R. Soc. London A* **102**, 161 (1922).
 - [6] G. Batchelor and J. Green, The determination of the bulk stress in a suspension of spherical particles to order c^2 , *J. Fluid Mech.* **56**, 401 (1972).

- [7] É. Guazzelli and O. Pouliquen, Rheology of dense granular suspensions, *J. Fluid Mech.* **852**, P1 (2018).
- [8] I. M. Krieger and T. J. Dougherty, A mechanism for non-Newtonian flow in suspensions of rigid spheres, *Trans. Soc. Rheol.* **3**, 137 (1959).
- [9] A. Sierou and J. F. Brady, Rheology and microstructure in concentrated noncolloidal suspensions, *J. Rheol.* **46**, 1031 (2002).
- [10] K. Yeo and M. R. Maxey, Dynamics of concentrated suspensions of non-colloidal particles in couette flow, *J. Fluid Mech.* **649**, 205 (2010).
- [11] E. Bertevas, X. Fan, and R. I. Tanner, Simulation of the rheological properties of suspensions of oblate spheroidal particles in a Newtonian fluid, *Rheol. Acta* **49**, 53 (2010).
- [12] B. Snook, J. Butler, and É. Guazzelli, Dynamics of shear-induced migration of spherical particles in oscillatory pipe flow, *J. Fluid Mech.* **786**, 128 (2016).
- [13] C. J. Lin, J. H. Peery, and W. Schowalter, Simple shear flow round a rigid sphere: inertial effects and suspension rheology, *J. Fluid Mech.* **44**, 1 (1970).
- [14] G. Subramanian, D. L. Koch, J. Zhang, and C. Yang, The influence of the inertially dominated outer region on the rheology of a dilute dispersion of low-Reynolds-number drops or rigid particles, *J. Fluid Mech.* **674**, 307 (2011).
- [15] G. Subramanian and D. L. Koch, Inertial effects on fibre motion in simple shear flow, *J. Fluid Mech.* **535**, 383 (2005).
- [16] V. Dabade, N. K. Marath, and G. Subramanian, The effect of inertia on the orientation dynamics of anisotropic particles in simple shear flow, *J. Fluid Mech.* **791**, 631 (2016).
- [17] N. K. Marath and G. Subramanian, The inertial orientation dynamics of anisotropic particles in planar linear flows, *J. Fluid Mech.* **844**, 357 (2018).
- [18] G. Subramanian and D. L. Koch, Inertial effects on the orientation of nearly spherical particles in simple shear flow, *J. Fluid Mech.* **557**, 257 (2006).
- [19] M. Daghooghi and I. Borzjani, The influence of inertia on the rheology of a periodic suspension of neutrally buoyant rigid ellipsoids, *J. Fluid Mech.* **781**, 506 (2015).
- [20] H. Haddadi and J. F. Morris, Microstructure and rheology of finite inertia neutrally buoyant suspensions, *J. Fluid Mech.* **749**, 431 (2014).
- [21] K. Yeo and M. R. Maxey, Dynamics and rheology of concentrated, finite-Reynolds-number suspensions in a homogeneous shear flow, *Phys. Fluids* **25**, 053303 (2013).
- [22] P. M. Kulkarni and J. F. Morris, Suspension properties at finite Reynolds number from simulated shear flow, *Phys. Fluids* **20**, 040602 (2008).
- [23] D. Qi and L. Luo, Rotational and orientational behaviour of three-dimensional spheroidal particles in couette flows, *J. Fluid Mech.* **477**, 201 (2003).
- [24] H. Huang, X. Yang, M. Krafczyk, and X. Y. Lu, Rotation of spheroidal particles in couette flows, *J. Fluid Mech.* **692**, 369 (2012).
- [25] T. Rosén, F. Lundell, and C. K. Aidun, Effect of fluid inertia on the dynamics and scaling of neutrally buoyant particles in shear flow, *J. Fluid Mech.* **738**, 563 (2014).
- [26] T. Rosén, M. Do-Quang, C. K. Aidun, and F. Lundell, Effect of fluid and particle inertia on the rotation of an oblate spheroidal particle suspended in linear shear flow, *Phys. Rev. E* **91**, 053017 (2015).
- [27] T. Rosén, M. Do-Quang, C. K. Aidun, and F. Lundell, The dynamical states of a prolate spheroidal particle suspended in shear flow as a consequence of particle and fluid inertia, *J. Fluid Mech.* **771**, 115 (2015).
- [28] H. Huang, Y. F. Wu, and X. Y. Lu, Shear viscosity of dilute suspensions of ellipsoidal particles with a lattice Boltzmann method, *Phys. Rev. E* **86**, 046305 (2012).
- [29] J. Kromkamp, D. T. M. van den Ende, D. Kandhai, R. G. M. van der Sman, and R. M. Boom, Shear-induced self-diffusion and microstructure in non-Brownian suspensions at non-zero Reynolds numbers, *J. Fluid Mech.* **529**, 253 (2005).
- [30] C. K. Aidun, Y. Lu, and E.-J. Ding, Direct analysis of particulate suspensions with inertia using the discrete Boltzmann equation, *J. Fluid Mech.* **373**, 287 (1998).

- [31] S. K. Kang, Immersed boundary methods in the lattice Boltzmann equation for flow simulation, Ph.D. thesis, Texas A & M University (2012).
- [32] Z. Guo, C. Zheng, and B. Shi, Discrete lattice effects on the forcing term in the lattice Boltzmann method, [Phys. Rev. E](#) **65**, 046308 (2002).
- [33] Z.-G. Feng and E. E. Michaelides, The immersed boundary-lattice Boltzmann method for solving fluid-particles interaction problems, [J. Comput. Phys.](#) **195**, 602 (2004).
- [34] J. Kromkamp, D. van den Ende, D. Kandhai, R. van der Sman, and R. Boom, Lattice Boltzmann simulation of 2D and 3D non-Brownian suspensions in Couette flow, [Chem. Eng. Sci.](#) **61**, 858 (2006).
- [35] G. Batchelor, The stress system in a suspension of force-free particles, [J. Fluid Mech.](#) **41**, 545 (1970).
- [36] A. Kumar and J. J. Higdon, Dynamics of the orientation behavior and its connection with rheology in sheared non-Brownian suspensions of anisotropic dicolloidal particles, [J. Rheol.](#) **55**, 581 (2011).
- [37] A. Sierou and J. F. Brady, Shear-induced self-diffusion in non-colloidal suspensions, [J. Fluid Mech.](#) **506**, 285 (2004).
- [38] G. Drazer, J. Koplik, B. Khusid, and A. Acrivos, Deterministic and stochastic behaviour of non-Brownian spheres in sheared suspensions, [J. Fluid Mech.](#) **460**, 307 (2002).